energies

MDPI

Article

Two-Phase Flow Simulation of Multi-Droplet Motion Relevant for Polymer Electrolyte Fuel Cell Gas Channel Using the Volume of Fluid Approach

Dunke Liu [1,2,*], Dieter Froning [1] and Ralf Peters [1,2]

[1] IET-4: Institute of Electrochemical Process Engineering, Forschungszentrum Jülich GmbH, 52425 Jülich, Germany; ra.peters@fz-juelich.de (R.P.)
[2] Faculty of Mechanical Engineering, Ruhr-Universität, 44721 Bochum, Germany
* Correspondence: du.liu@fz-juelich.de

Abstract

This study develops a 3D computational fluid dynamics model of a polymer electrolyte fuel cell cathode gas channel with seven discrete liquid breakthrough inlets, one gas inlet, and a two-phase outlet. Two-phase flow and droplet evolution on the gas diffusion layer are simulated using the volume-of-fluid method in OpenFOAM. The model agrees well with reported experimental and numerical data in terms of droplet size, morphology, and detachment behavior. Results show that breakthrough geometry governs droplet dynamics: circular openings promote stronger aerodynamic loading and earlier detachment, while sharp-cornered geometries (e.g., triangular and polygonal) stabilize droplets and prolong residence time. Among all investigated geometries, the circular breakthrough exhibits the highest drainage efficiency, in agreement with recent experimental studies demonstrating that laser-drilled circular pores facilitate water removal and reduce oxygen mass-transfer resistance in polymer electrolyte fuel cells. Complex interactions with the gas diffusion layer surface, gas channel walls, and corners lead to coalescence, sliding, and rivulet formation. Force decomposition reveals the competition among aerodynamic, capillary, adhesion, and shear forces. The study provides a mechanistic basis for geometry-controlled water transport and guidance for gas diffusion layer design and water management.

Keywords: polymer electrolyte fuel cells; modeling; gas diffusion layer surface; force analysis; water management

Academic Editors: Song Li and Ivan Tolj

Received: 3 July 2026
Revised: 28 July 2026
Accepted: 29 July 2026
Published: 1 August 2026

1. Introduction

With increasing concern about energy security, air pollution, and global warming, the potential use of polymer electrolyte fuel cell (PEFC) in future sustainable and renewable energy systems has gained considerable momentum [1–3]. The principles of PEFC technology can be traced back to the 19th century, and after nearly two centuries of development, PEFC has become the most promising type of fuel cell for automotive and some portable applications. Due to their high-power density and low operating temperature, PEFCs are also considered to have potential for backup power and distributed energy applications.

Despite significant progress in engineering and science, large-scale commercialization of PEFC has not been achieved in the past few decades, with major obstacles including: (1) technical issues related to water management; (2) high costs of materials and components [4–6]. Among these, water management is a key factor affecting fuel cell performance and durability. Understanding the complexity of this problem lies in the strong coupling

of heat and mass-transfer processes, the existence of two-phase flow and phase transition phenomena in porous media, and the complex transport and accumulation behavior of liquid water between different layers. Water generated by electrochemical reactions may condense and form droplets within the gas diffusion layer (GDL) or gas channel. If these droplets are not drained in time, they will cause gas channel blockage, localized oxygen deficiency, uneven current distribution, and performance degradation. Therefore, a deep understanding of the generation, transport, and evolution of liquid water is crucial for the further development of PEFC technology [7–10].

Computational fluid dynamics (CFD) methods provide an important tool for studying heat and mass transfer and two-phase flow in fuel cells. Numerical simulations can significantly reduce experimental costs and time and reveal transient interface evolution processes that are difficult to capture experimentally. CFD-based fuel cell models can not only be used to verify experimental results but also to evaluate the impact of different gas channel structures, operating parameters, and material properties on performance during the design phase [11,12]. However, many assumptions are typically made when building models, such as the interaction between gas and liquid, wall wettability, and effective parameters of porous media. This makes the simulation results quite sensitive to boundary conditions and properties.

A typical PEFC flow field consists of a series of gas channels. Effective removal of liquid water from the cathode side remains a key challenge. Since oxygen diffuses into the reaction interface within the cathode gas channel, droplet accumulation in the gas channel will hinder gas-phase transport and lead to local flooding, resulting in performance degradation or even operational instability [4,10,13]. Liquid water typically seeps from the GDL surface and enters the gas channel as droplets or thin films. Its dynamic behavior is influenced by factors such as gas channel geometry, gas velocity, wall wettability, and droplet size and distribution. When the gas momentum is sufficient to overcome surface tension, droplets may be carried out of the gas channel in the form of slug flow, mist flow, or wall film/corner flow [14,15]. Appropriate design of the gas channel geometry and wall contact angle can achieve efficient drainage at lower pressure drops.

Although extensive experimental and numerical studies have been conducted to understand liquid water transport in PEFC gas channels, several important gaps remain. The majority of current simulations adopt simplified breakthrough geometries—typically circular, uniform, or single-point liquid inlets—overlooking the inherent heterogeneity and anisotropy of real GDL fibrous structures, which naturally produce irregular, orientation-dependent breakthrough morphologies [16,17]. Furthermore, multi-point breakthrough, a common occurrence in practical GDL that critically governs droplet coalescence, shielding effects, and detachment dynamics, has seldom been researched through systematic experiments and modeling. Consequently, the combined influence of inlet geometry, inlet orientation, breakthrough size, gas velocity, and wall/GDL wettability remains insufficiently understood [18–20]. A systematic analysis of how the shape of breakthrough openings affects droplet dynamics under multiple simultaneous breakthrough sites in the gas flow channel of a PEFC—a condition typical of real GDL—is still lacking.

Recent experimental studies have shown that introducing engineered pores into GDL can significantly improve water removal and mass transport. Horst et al. [21] used a carbon dioxide laser to create arrays of cylindrical (approximately circular) pores in GDL, reducing oxygen mass-transfer resistance by 28% and increasing the current density at 0.7 V by 18%. Similarly, Peng et al. [22] fabricated aligned pore channels that promoted rapid liquid water transport, leading to substantial performance improvements in direct methanol fuel cells and zinc–air cells. These studies indicate that regular pore-engineered pathways, typically realized as circular laser-drilled holes, can facilitate liquid water drainage and alleviate

flooding. However, the underlying role of breakthrough geometry itself has not been systematically investigated, and it remains unclear whether circular pores outperform other possible inlet shapes and through what physical mechanisms. Lv et al. [23] combined micro-CT reconstructed GDL structures with LBM simulations to develop a droplet detachment model for PEMFCs, identifying 120–140° as the optimal intrinsic contact angle range for water removal and establishing the minimum necking diameter of the liquid bridge as the characteristic length governing the critical detachment force. Aroge et al. [24] proposed rapid operando X-ray radiography as a complement to 3D computed tomography for PEFC liquid water visualization, revealing initial transient water buildup, random breakthrough point behavior with ~54% average persistence, and demonstrating a high-resolution, minimally intrusive lab-based workflow that extends X-ray imaging capabilities. Pei et al. [25] designed a visualization setup for PEFC gas channels and experimentally observed that the volume and number of liquid droplets initially increased, followed by the coalescence of small droplets into larger ones.

Despite these important advances, several fundamental questions about liquid water breakthrough from realistic GDL structures remain unresolved. In particular, it is not yet clear how the intrinsic heterogeneity of fibrous media governs the emergence, morphology, and transport behavior of liquid water at the GDL–gas channel interface. Motivated by these observations, this work develops a three-dimensional volume-of-fluid (VOF) model of a gas channel incorporating seven independent liquid breakthrough sites on the GDL surface with five distinct inlet geometries (triangular, square, pentagonal, hexagonal, and circular), thereby closely mimicking the geometric diversity arising from random fibrous microstructures. The model is validated against experimental data in terms of droplet shape evolution, growth behavior, and detachment time. A comprehensive parametric study is then conducted to elucidate how breakthrough geometry, inlet size, number of inlets, gas velocity, and surface wettability jointly govern droplet transport behaviors, including sidewall flow, corner flow, top-wall flow, and GDL-surface flow. Furthermore, detailed force decomposition analysis (including inertial, pressure, capillary, and viscous forces) is performed to reveal the underlying mechanisms driving different flow regimes. These findings provide new physical insights into multi-point water breakthrough phenomena and offer valuable guidance for the design of PEFC flow fields and GDL structures with improved water management capability.

2. Mathematical Model

A three-dimensional computational model was developed to investigate two-phase flow behavior in a single-gas channel PEFC. The model consists of a straight gas channel coupled with a GDL area, in which localized liquid water breakthrough regions are explicitly resolved. Dry air is supplied through a single gas inlet at the gas channel entrance, while a two-phase mixture of air and liquid water exits through the gas channel outlet. Liquid water is introduced into the gas channel exclusively through predefined breakthrough areas on the GDL surface, representing water emerging from the porous electrode under operating conditions.

2.1. General Assumptions

- Both gas and liquid phases are treated as incompressible and immiscible, and the simulations are performed under isothermal conditions at 80 °C.
- The GDL is represented as a liquid source on its upper surface, with its internal pore-scale transport not explicitly resolved.
- Liquid water enters the gas channel through prescribed discrete breakthrough inlets with steady injection velocities.

– Electrochemical reactions, species transport, and in situ water generation are not considered, and the focus is placed solely on droplet hydrodynamics after breakthrough. Consequently, the results reflect post-breakthrough hydrodynamics rather than the full coupled behavior of an operating cell. It is assumed that the imposed liquid inlet velocities correspond to local breakthrough intensities, rather than to PEFC averaged current densities.
– Phase change was not considered.

2.2. VOF Model

The VOF model [26] is an interface analysis method that has become a commonly used approach for solving two-phase flow phenomena within PEFC [27–29]. Using the VOF method, the interphase interface is tracked by the volume fraction of liquid water in the computational cell volume scheme. According to the VOF method, in each cell of the mesh, each dependent variable has only one value defining the state. A function α (*alpha.water*) is introduced, whose value is 1 wherever the liquid phase occupies the area, and zero otherwise [30]:

$$\alpha = \frac{V_l}{V_{CV}} \tag{1}$$

V_l is the volume of the calculated element, and V_{CV} is the volume of the liquid phase. In three-dimensional space, the fractional equation for the water phase follows [26]:

$$\frac{\partial \alpha}{\partial t} + u\frac{\partial \alpha}{\partial x} + v\frac{\partial \alpha}{\partial y} + w\frac{\partial \alpha}{\partial z} = 0 \tag{2}$$

The α value moves with the fluid.

The governing equations are the continuity and momentum equations that have the following form:

$$\frac{\partial \rho}{\partial t} + \nabla \cdot (\rho v) = 0 \tag{3}$$

$$\frac{\partial (\rho v)}{\partial t} + \nabla \cdot (\rho v v) = -\nabla p + \mu \nabla^2 v + \rho g + F \tag{4}$$

where g is the acceleration due to gravity, and F is the source term representing surface tension. The v vector can be defined as [29]:

$$v = \frac{\alpha \rho_l v_l + (1-\alpha)\rho_g v_g}{\alpha \rho_l + (1-\alpha)\rho_g} \tag{5}$$

The pressure drop across the entire surface is a function of the surface tension (γ) [27]:

$$\Delta p = \gamma \left(\frac{1}{R_1} + \frac{1}{R_2} \right) \tag{6}$$

Here, R_1 and R_2 are the two orthogonal radii required to measure surface curvature. According to the Continuous Surface Force (CSF) method, surface tension can be expressed as a pressure jump across the interface, and in the momentum equation, it is represented as a body force [27]:

$$F(\mathrm{CSF}) = \gamma k \frac{\rho \nabla s_l}{(\rho_l + \rho_g)/2} \tag{7}$$

where k is the surface curvature, which can be defined based on the divergence of the interface normal unit vector (n) [27,28]:

$$k = \nabla \cdot n = \nabla \cdot (n_w \cos\theta_w + t_w \sin\theta_w) \tag{8}$$

Here, we have the unit vector tangent to the wall, the unit vector normal to the wall, and the static contact angle of the wall.

2.3. Force Analysis

After liquid water breaks through the GDL surface into the gas channel, droplet motion is governed by the competition among several forces, including aerodynamic inertial force ($F_{p,x}$, $F_{p,y}$, $F_{p,z}$), viscous shear force ($F_{\mu,x}$, $F_{\mu,y}$, $F_{\mu,z}$), surface tension, and adhesion ($F_{\sigma,x}$, $F_{\sigma,y}$, $F_{\sigma,z}$) at the three-phase contact line.

Under gas flow, the aerodynamic inertial force originates from the pressure difference between the windward and leeward sides of the droplet and represents the primary driving force for droplet migration and detachment. Its streamwise component (x-direction in Figure 1) governs downstream transport, whereas geometric asymmetry of the breakthrough opening or proximity to the sidewall can generate pronounced transverse or vertical components, leading to lateral deflection or lift-induced motion. Viscous shear forces acting at the gas–liquid interface and liquid–solid contact regions contribute to droplet deformation and sliding along the wall or GDL surface but are generally insufficient to overcome resistance on their own.

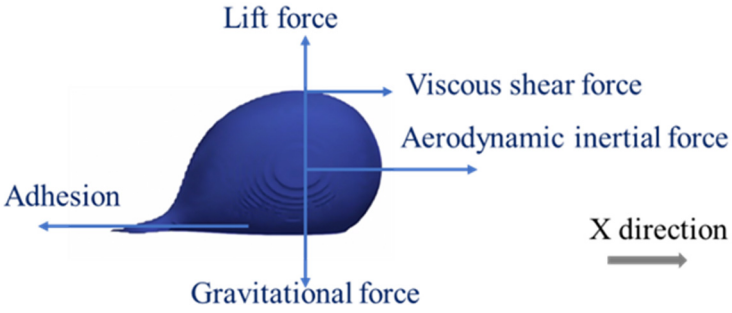

Figure 1. Force analysis of the droplet.

Surface tension stabilizes the droplet interface by maintaining curvature continuity and constitutes the dominant resisting force against deformation and detachment. At the three-phase contact line, surface tension combined with surface wettability gives rise to an adhesion force, which depends on the contact angle and contact-line length. Increasing the hydrophobicity of the GDL surface reduces this adhesion force and facilitates earlier droplet detachment.

Accordingly, droplet detachment and subsequent transport occur only when the combined aerodynamic inertial and viscous forces exceed the resisting effects of surface tension and adhesion. Figure 1 schematically illustrates the major forces acting on the droplet and their directional decomposition, providing a unified physical basis for the analysis of different flow regimes discussed in the following sections.

According to Newton's second law (The following equations are all in the *x*-axis direction):

$$\rho_i V_i \frac{\partial u_i}{\partial t} = \left(F_{P,x} + F_{\mu,x} - F_{\mu,s} - F_{\sigma,x}\right) \tag{9}$$

The aerodynamic inertial force [31]:

$$F_{P,x} = \int_{A_x} n_x P_x dA_x \tag{10}$$

$$F_{P,y} = \int_{Ay} n_y P_y dA_y \tag{11}$$

$$F_{P,z} = \int_{Az} n_z P_z dA_z \tag{12}$$

Fluid–fluid viscous shear force [31]:

$$F_{\mu,x} = \int_A \mu n_y \cdot \nabla u_x dA + \int_A \mu n_z \cdot \nabla u_x dA \tag{13}$$

Adhesion force [31]:

$$F_{\sigma,x} = \int_{L\sigma} \sigma n_x \cos\theta dL\sigma \tag{14}$$

$$F_{\sigma,y} = \int_{L\sigma} \sigma n_y \cos\theta dL\sigma \tag{15}$$

$$F_{\sigma,z} = \int_{L\sigma} \sigma n_z \cos\theta dL\sigma \tag{16}$$

where A is the area; A_x, A_y, A_z are the projected area of the droplet in the xyz direction; ρ_i is the density of water; V_i is the volume of water; u_i is the velocity of water; t is the time; $F_{\mu,x}$ is the component of viscous force along the x-axis; $F_{\mu,s}$ is the component of fluid–solid viscous shear force along the x-axis; P_x, P_y, P_z are the components of pressure along the xyz axis; $P_x = P_y = P_z$, n_x, n_y, n_z are the unit vectors; $F_{\sigma,x}, F_{\sigma,y}, F_{\sigma,z}$ are the components of adhesion along the xyz axis; $L\sigma$ is the gas–solid contact line between the droplet and the GDL surface; σ is the surface tension; and θ is the contact angle.

The droplet forces were evaluated using ParaView-5.13.1's surface and volume integration workflow. At each time step, the liquid phase was identified from the volume fraction field, and the liquid–gas interface together with the wetted wall surfaces was extracted. ParaView-5.13.1 integration filters were then applied to quantify the force components by spatially integrating the relevant fields. The inertial force was obtained from the pressure and momentum flux acting on the droplet interface, the viscous shear force from the tangential stress distribution, the surface-tension force from curvature-dependent capillary stresses, and the adhesion force from capillary traction along the three-phase contact line. All forces were decomposed into streamwise, transverse, and vertical components to enable direct comparison of their relative contributions to droplet deformation, detachment, and migration, as seen in Figure 1.

2.4. Model and Parameters

Table 1 summarizes the modeling parameters employed in this study and their correspondence to representative PEFC operating conditions. Distinct wettability conditions are prescribed for the graphite gas channel wall (contact angle 53°) and the GDL surface (124°/140°/153°), reflecting typical hydrophilic–hydrophobic contrasts in PEFC components. Fluid properties are taken as standard values for air–water systems under typical operating conditions.

The imposed gas and liquid inlet conditions are selected to represent physically consistent operating regimes of a practical PEFC. The gas inlet velocities of 5, 10, and 15 $m \cdot s^{-1}$ are scaled to a cell with an active area of 200 cm^2 and 25 parallel cathode gas channels. Assuming a mean current density of 1.0 $A \cdot cm^{-2}$, these velocities correspond to oxygen stoichiometric ratios of approximately 0.5 (lack of air), 1.0 (low stoichiometry), and 1.5 (medium stoichiometry), respectively, under ambient pressure. Consequently, the selected gas velocities span oxygen-deficient, low-stoichiometry, and moderate-stoichiometry cathode operation, which are particularly relevant for examining liquid water accumulation, droplet detachment, and drainage behavior in the PEFC gas channel.

Table 1. Modeling parameters [19].

Type	Value
Gas channel length	1.34×10^{-2} m
Gas channel height	3×10^{-4} m
Gas channel width	8×10^{-4} m
Contact angle GC wall (average)	53°
Contact angle GDL surface (average)	124°/140°/153°
Gas velocity	5/10/15 m·s^{-1}
Reynolds number	144/289/433
Mach number	0.015/0.029/0.044
Liquid inlet velocity	0.0209/0.1045/0.2090 m·s^{-1}
Density water	988 kg·m^{-3}
Density air	1.205 kg·m^{-3}
Viscosity water	1.004×10^{-6} m^2·s^{-1}
Viscosity air	1.511×10^{-5} m^2·s^{-1}
Surface tension	0.07197 N·m^{-1}

Seven circular breakthrough inlets with a radius of 33 µm are prescribed, yielding a total inlet area of 2.39×10^{-8} m^2. Based on Faraday's law and a gas channel active area of 8 cm^2 (corresponding to a 200 cm^2 cell with 25 parallel gas channels), the imposed liquid inlet velocities correspond to local equivalent current densities of approximately 0.66, 3.31, and 6.61 A·cm^{-2}, respectively. These values represent localized water generation intensities associated with breakthrough regions rather than cell-averaged current densities.

2.5. Model Development

The present model treats the GDL surface as a liquid source to study breakthrough behavior at the GDL–gas channel interface, extending prior single-droplet studies [18,19]. To capture realistic heterogeneous water emergence, seven discrete breakthrough sites are prescribed along the interface based on Yu's statistical results [32,33], with varied geometric shapes (triangles, squares, pentagons, hexagons, circles) mimicking irregular pores of Toray-90 GDL [20]. These inlets are organized into seven GDL sub-regions, each containing 1–4 breakthrough sites, enabling systematic investigation of inlet number density and spatial clustering. The model resolves simultaneous droplet growth, interaction, coalescence, and detachment at multiple locations, bridging idealized single-inlet and realistic PEFC two-phase flow.

The straight gas channel is 13.4 mm long and 0.8 mm wide, with a GDL region on the bottom wall starting 3 mm downstream of the inlet and covering the central portion, Figure 2a. The channel comprises an inlet region, a GDL–droplet region, and a fully developed region. Seven breakthrough inlets are numbered sequentially and grouped into three: Group I (inlets 1–3) upstream near one sidewall, Group II (4–5) mid-channel, and Group III (6–7) downstream near the opposite sidewall, allowing analysis of location-dependent droplet interactions and airflow development, Figure 2b.

Air enters from the left and flows over the GDL; water is injected through the seven breakthroughs to mimic GDL liquid transport. By resolving droplet interactions among groups, the model captures combined effects of breakthrough location, droplet–droplet dynamics, and evolving gas flow conditions, while the varied inlet shapes and sub-region densities systematically bridge single-inlet idealizations and practical PEFC behavior.

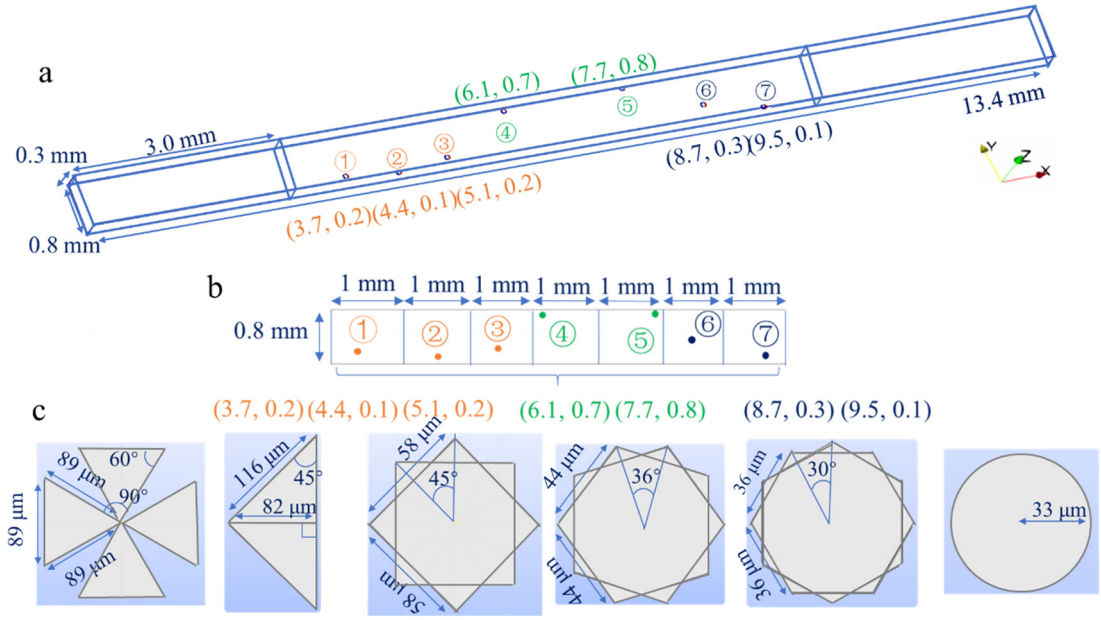

Figure 2. Droplet breakthrough shape, angle, size, coordinate, and gas channel. (**a**) Gas channel dimensions. (**b**) GDL region is divided into seven parts; breakthrough coordinates, yellow: group 1, green: group 2, blue: group 3. (**c**) Breakthrough shape and angle; different breakdown shapes correspond to different angles, and all breakdown shapes contain the same area.

2.6. Mesh Dependency Study

A mesh independence study was performed to ensure that the numerical predictions of droplet morphology, growth behavior, and detachment dynamics were not influenced by mesh resolution. Five structured hexahedral mesh configurations were generated, with characteristic cell sizes of 60, 45, 35, 25, and 15 μm, respectively. For each grid, the complete transient VOF simulation was conducted under identical operating and boundary conditions, and the droplet evolution was examined at several characteristic time instants (1 ms, 3 ms, 8 ms, and 12 ms). For coarse meshes with cell sizes $\geq$ 35 μm, the simulations consistently failed to capture the liquid–gas interface. The droplets were numerically dispersed shortly after emerging from the breakthrough points, indicating excessive numerical diffusion of the volume fraction field. Such artificial breakup prevented the prediction of physically meaningful droplet growth or detachment processes. When the mesh size was reduced to 25 μm in Figure 3, the interface became continuous and droplet growth was qualitatively captured; however, the predicted detachment time and interface curvature still deviated from experimental observations due to insufficient spatial resolution near the contact line. Only the finest mesh with a characteristic size of 15 μm in Figure 3 successfully reproduced all experimentally observed features all the time [18], including the progressive droplet expansion on the GDL surface, the moment of detachment, and the post-detachment trajectory [19]. The droplet size and detachment time obtained from this mesh showed excellent agreement with high-speed imaging data [18], confirming that this resolution is sufficient for accurately resolving the interfacial curvature, capillary forces, and the competition between inertial and surface-tension effects. Based on this systematic assessment, the 15 μm mesh was selected for all subsequent simulations. While this refinement significantly increases computational cost, it ensures that the delicate interface dynamics and capillary-dominated physics are faithfully represented.

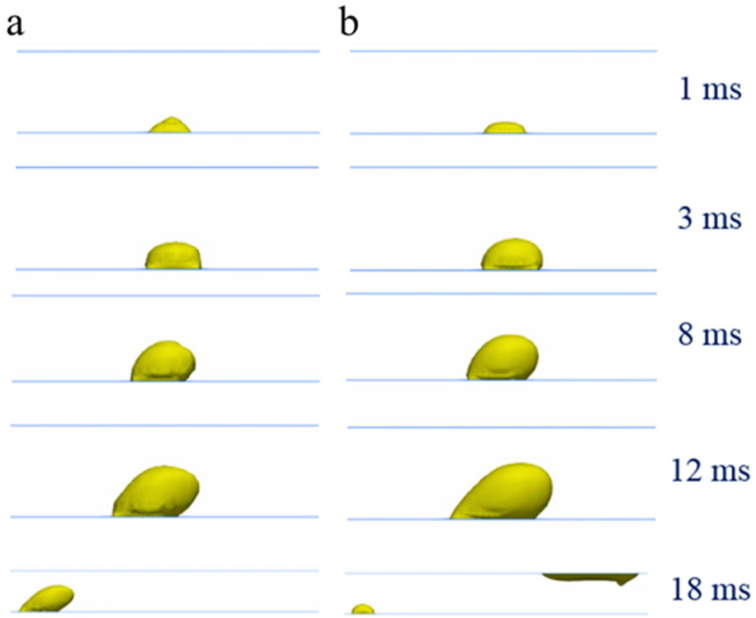

Figure 3. Simulated droplet outflow, detached from GDL, droplet morphology at different times when the side length of the hexahedral mesh is 25 μm (**a**) and 15 μm (**b**).

2.7. Adaptive Refine Mesh

An adaptive mesh refinement (AMR) strategy based on the OpenFOAM-11 dynamic mesh method was applied using a background cell size of 0.02 mm, one refinement layer, and a maximum of two refinement levels, enabling over an order-of-magnitude reduction in cell count while preserving interface resolution and droplet dynamics comparable to a uniform fine mesh.

2.8. Boundary Conditions and Solver Settings

OpenFOAM-11 software was used, with the interFoam solver [34,35]. Geometric parameters and physical properties are defined in Table 1. Adjustable runtime was used, and the maximum Courant number (*Co*, Equation (17)) and maximum alpha Courant number (*alphaCo*, Equation (18)) were defined as 0.5 and 0.7, respectively.

$$Co = \frac{|u|\Delta t}{\Delta x} \tag{17}$$

$$alphaCo = \frac{\Delta t \cdot \sum |phi\_f|}{V \cdot \max(alpha.water, \text{smallnumber})} \tag{18}$$

where u is the fluid velocity; Δt is the current time step; Δx is the mesh feature size; $|phi\_f|$ is the flux of the mesh surface; V is the mesh volume; *alpha.water* is the phase fraction of the current mesh (0–1); and ε is the small number to avoid the denominator being 0 when *alpha.water* ≈ 0. The small number, typically 10^{-12}, is a numerical stability parameter to prevent the denominator from becoming zero.

For the gas and liquid inlets, uniform velocities with given average values were defined (according to Table 1). Zero gradient was used at the outlet, with no-slip velocity on the wall. For pressure, the outlet was defined as a fixed value (zero), and all other boundaries were set to zero gradient. The boundary conditions for *alpha.water* were defined as follows: gas inlet as uniform (value 0), outlet as zero gradient, gas channel wall as a contact angle of 53°, GDL surface as a contact angle of 140° (but this varies in the parameter study), and liquid inlet as uniform (value 1).

For all simulations in the parameter study, the scotch method was used to decompose the domain, suitable for 48 CPUs. The mesh used in this study achieved optimal computational speed with 48 CPUs. Table 2 shows that adaptive meshing can save 75% of core time.

Table 2. Different meshing methods.

	Global Fine Mesh	Adaptive Refine Mesh
Meshes	6,197,500	405,479
CPUs	192	48
Background mesh size	8×10^{-6} m	2×10^{-5} m
Core-h	46,080	3456

The VOF simulations serve as a virtual counterpart to physical experiments, leveraging high-performance computing (HPC) resources. The resultant datasets are expected to inform macroscopic upscaling approaches, such as pore-network modeling (PNM), which can be executed on conventional computational workstations.

3. Results and Discussion

3.1. Effects of Air Velocity, Water Velocity, Inlet Size, Wettability, and Number of Breakthrough Inlets

3.1.1. Water Velocity

Figure 4a reports the detachment time at each of the seven breakthrough locations for three water injection velocities (0.0209, 0.1045, and 0.2090 m/s) at a fixed air velocity of 10 m/s. Raising the water velocity by an order of magnitude reduces the detachment time at every location by a comparable proportion—for example, from ≈0.094 s to ≈0.011 s at location ①—while the qualitative location-to-location pattern is essentially preserved at all three velocities: locations ①–③ and ⑥–⑦ remain longer, and locations ④–⑤ remain markedly shorter, irrespective of the water velocity imposed. This near-uniform rescaling indicates that water velocity governs primarily the rate at which the droplet accumulates volume, rather than the underlying detachment mechanism or its spatial distribution: a higher injection rate simply shortens the time required to reach the critical volume for detachment at every location by a similar factor. This trend agrees with the findings of Andersson et al. [19].

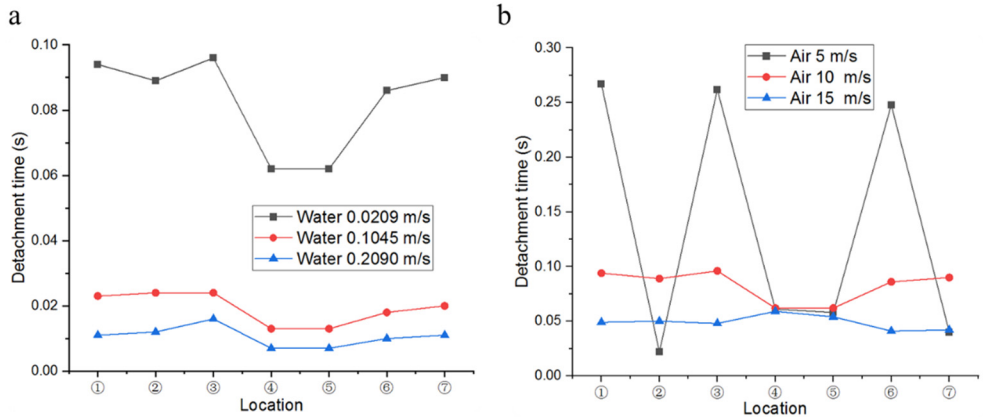

Figure 4. Effect of water and air injection velocity on droplet detachment time at the seven breakthrough locations defined in Figure 2a. (**a**) Detachment time for three water velocities (0.0209, 0.1045 and 0.2090 m/s) at a fixed air velocity of 10 m/s. (**b**) Detachment time for three air velocities (5, 10 and 15 m/s) at a fixed water velocity of 0.0209 m/s.

3.1.2. Air Velocity

Figure 4b reports the detachment time at each location for three air velocities (5, 10 and 15 m/s) at a fixed water velocity of 0.0209 m/s. At the two higher air velocities (10 and 15 m/s), the detachment time is comparatively short and varies smoothly with location, consistent with an aerodynamic-drag-dominated release mechanism operating independently at each inlet. At the lowest air velocity examined (5 m/s), by contrast, the response becomes strongly non-monotonic: locations ①, ③ and ⑥ exhibit greatly extended detachment times (≈0.25–0.27 s), location ② exhibits an anomalously short detachment time (≈0.02 s), and locations ④, ⑤ and ⑦ remain moderate (≈0.04–0.06 s). This behavior suggests that, when the aerodynamic loading is too weak to shed each droplet independently within a short interval, detachment instead becomes contingent on the stochastic timing of coalescence with a neighboring droplet: locations that must await such a merging event before the combined structure attains sufficient volume, and momentum to detach (①, ③, ⑥) show substantially prolonged detachment times, whereas the markedly short time recorded at location ② is consistent with an early, favorably timed coalescence event in this particular simulation. As air velocity increases to 10–15 m/s, aerodynamic drag becomes sufficient to detach each droplet independently within a comparable, shorter interval, without requiring coalescence, which accounts for the smoother, more uniform location profile observed at these conditions.

The results in Figure 2 reinforce the interpretation, developed in Section 3.2.1, that breakthrough location—and specifically proximity to the hydrophilic channel sidewall at locations 4 and 5—exerts a first-order influence on detachment behavior that persists across the full range of water and air velocities examined. The pronounced local minimum in detachment time at locations ④/⑤ is preserved at every water velocity in Figure 4a and at every air velocity in Figure 4b, including under the highly irregular, coalescence-dominated conditions at 5 m/s air velocity, where locations 4 and 5 nonetheless remain within the moderate range rather than exhibiting the extreme prolongation observed at locations 1, 3 and 6. This robustness indicates that the wall-wetting pathway available to droplets at locations 4/5 operates essentially independently of the operating flow conditions, whereas the aerodynamic- and coalescence-driven pathway that governs the remaining locations is comparatively sensitive to both water and, especially, air velocity.

3.1.3. Inlet Size

Figure 5a demonstrates that increasing the breakthrough radius from 0.0165 mm to 0.0660 mm lengthens the detachment time at every location, in certain cases by a factor of approximately four (e.g., location ①: 0.045 s at r = 0.0165 mm versus 0.188 s at r = 0.0660 mm). Although this trend may initially appear counter-intuitive—a larger opening might be expected to generate a destabilizing frontal area, and hence to promote detachment, more rapidly—it is consistent with the fact that all radii were simulated at an identical liquid injection rate: a larger inlet distributes the same volumetric flux over a wider base, such that the emerging droplet initially grows preferentially in lateral extent rather than in protruding height, and only gradually develops the curvature and frontal area required to initiate detachment. Because the capillary retention force scales with the pinned contact-line length, which itself increases with inlet radius, this retention effect further reinforces the observed delay. Notably, even at the largest radius examined, locations ④ and ⑤ remain among the fastest to detach (Figure 4a), indicating that the wall-wetting pathway identified in Section 3.2.1 for these two locations persists, and indeed dominates, across the full range of breakthrough radii considered.

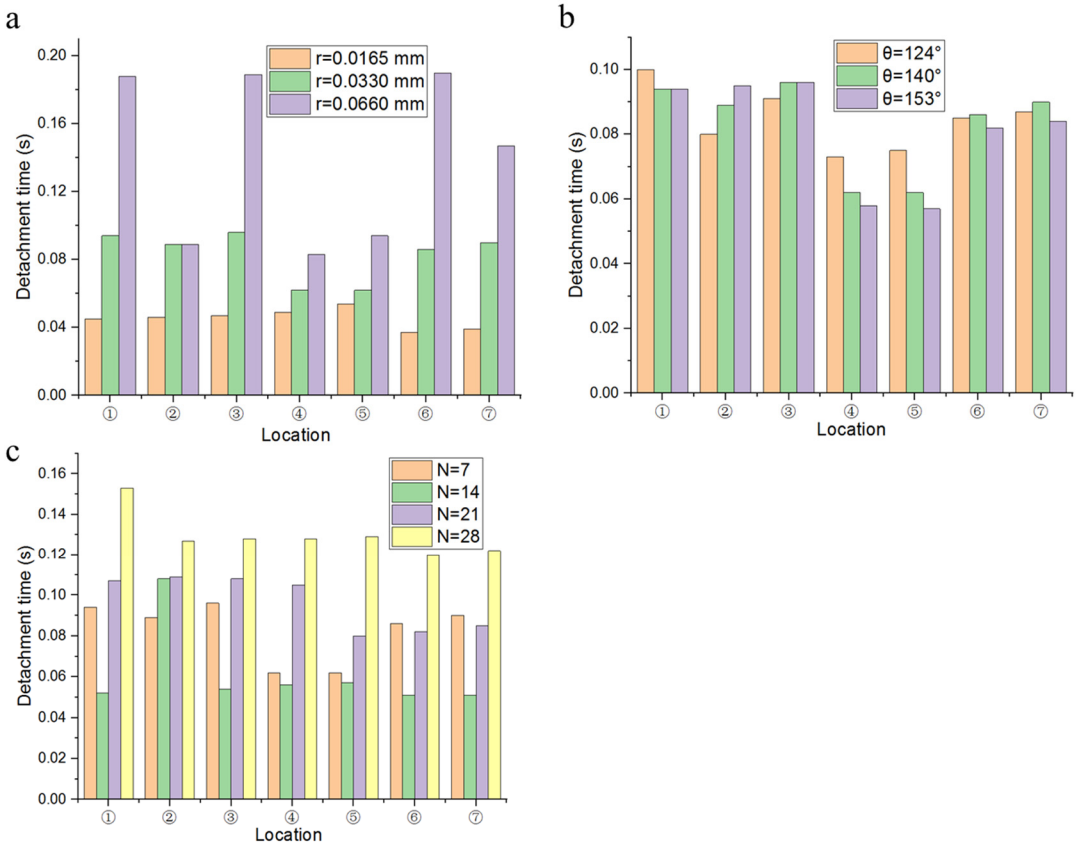

Figure 5. Parametric effects on droplet detachment time. (**a**) Breakthrough radius (r = 0.0165, 0.0330 and 0.0660 mm), resolved by location. (**b**) GDL contact angle (θ = 124°, 140° and 153°), resolved by location. (**c**) Number of active breakthrough inlets (N = 7, 14, 21 and 28), resolved by location.

3.1.4. Wettability (Contact Angle)

The contact angle at the GDL–gas channel interface was chosen based on physically realistic apparent wetting behavior reported for liquid water emerging from fibrous GDL structures. Yu et al. [17] showed that droplets breaking through stochastic GDL microstructures exhibit highly asymmetric shapes and view-angle-dependent apparent contact angles, typically ranging from approximately 120° to 150°. Figure 5b indicates that the influence of GDL contact angle on detachment time is markedly location-dependent rather than uniform across the channel. At locations ④ and ⑤, increasing the contact angle from 124° to 153° produces a clear, monotonic reduction in detachment time (≈ 0.073 → 0.058 s and ≈ 0.075 → 0.057 s, respectively), whereas at locations ①–③ and ⑥–⑦, detachment time varies only weakly and non-monotonically with contact angle. This contrast is consistent with, and adds mechanistic nuance to, the wall-proximity argument developed in Section 3.2.1: locations 4 and 5 lie close to the hydrophilic channel sidewall, so that the GDL contact angle and the (fixed) sidewall wettability act in combination to set the droplet's preferred wetting path. As the GDL is rendered progressively less wettable (higher contact angle), the droplet is increasingly disfavored from spreading on the GDL floor and is correspondingly more readily drawn toward the adjacent hydrophilic wall, reinforcing the wall-wetting route and further shortening detachment time at locations 4/5. At locations away from the hydrophilic sidewall (①–③, ⑥–⑦), no such competing wetting surface is available, so that detachment instead proceeds primarily through the aerodynamic- and coalescence-driven pathway described in Sections 3.1.1, 3.1.2 and 3.2.1, which is comparatively insensitive to GDL contact angle over the range examined.

3.1.5. Number of Breakthrough Inlets

Figure 5c shows that the number of active breakthrough inlets, N, affects detachment time in a non-monotonic manner: N = 14 gives the shortest detachment time at every location (≈0.05–0.06 s), N = 7 is intermediate (≈0.06–0.10 s), and N = 21 and N = 28 progressively increase the detachment time, with N = 28 giving the longest times observed in this study (up to ≈ 0.15 s at location ①). The elevated detachment times at high inlet density (N = 21, 28) are readily explained by the increased frequency of droplet merging identified in Section 3.2.1: as more inlets are activated, adjacent droplets are more likely to bridge into rivulets that must accumulate substantially more liquid before the combined structure sheds, extending the effective detachment time. The comparatively short detachment time at the lowest density tested here, N = 14, relative to the even sparser N = 7 case is less immediately obvious and may reflect a favorable inlet spacing at which neighboring droplets locally accelerate the crossflow passing between them (an aerodynamic-shielding or channeling effect) without yet being close enough to merge; this hypothesis is consistent with the absence of any merging events reported for locations ④ and ⑤ in Section 3.2.1.

3.2. Effects of Different Inlet Shapes

The breakthrough geometry strongly governs the initial boundary condition of the emerging liquid and therefore shapes the subsequent interfacial evolution, force balance, and detachment characteristics inside the gas channel. In general, geometries containing sharp corners or asymmetric windward faces introduce localized pressure gradients and non-uniform inertial loading, which accelerate deformation or early partial breakup. In contrast, rounded or axisymmetric geometries lead to smoother aerodynamic stress distributions and consequently more stable droplet growth and predictable detachment behavior. The detailed effects of each geometry are discussed below.

3.2.1. Triangular Inlets

Table 3 summarizes the pre-detachment contact footprint and the detachment volume of the droplet emerging from the first inlet for five triangular breakthrough orientations (Triangles 1–5, as defined in Figure 2c). The detachment volume ranges from 1.48 nL (Triangle 1) to 1.71 nL (Triangle 5), a variation of approximately 15% that is attributable solely to inlet orientation, given that the injected flow rate and the nominal opening area are otherwise identical across the five cases.

This orientation dependence may be rationalized through a force-balance argument: droplet detachment occurs once the streamwise aerodynamic drag acting on the exposed frontal area exceeds the capillary retention force pinned along the triangular contact line. Owing to the rotational asymmetry of a triangular perimeter, changing the inlet orientation simultaneously alters (i) the length of contact line presented broadside to the flow, which governs the magnitude of the retention force, and (ii) the degree to which the droplet base is skewed toward the upstream or downstream side, which governs the asymmetry of the interfacial pressure loading. When a sharp vertex is oriented into the oncoming flow, as for Triangle 1, the attached droplet adopts a more streamlined, lower-drag profile and is retained more effectively, resulting in detachment at the smallest volume within the set; conversely, when a flat edge or vertex trails the flow, as for Triangle 5, t despite promoting earlier local necking, requires greater volumetric accumulation before the asymmetric footprint becomes unstable, thereby yielding the largest detachment volume observed. The orientation dependence identified for triangular inlets is therefore governed by the coupled interplay between contact-line pinning and frontal-area drag, rather than by inlet size alone.

Table 3. Triangular breakthrough droplet detachment from GDL shape and volume. In the 2nd column of the table, light gray represents the breakdown shape, and green represents the three-phase contact profile of the droplet; the lower part represents the region near the gas channel wall.

	The Contact Shape Between the Droplet and the GDL Before the First Inlet Droplet Separation (1 ms)	Volume of the First Inlet Droplet When Separated (nL)
Triangle 1		1.48
Triangle 2		1.69
Triangle 3		1.50
Triangle 4		1.60
Triangle 5		1.71
Triangle 6		1.62

Table 4 extends the analysis of Table 3 to all seven breakthrough locations and to a sixth triangular orientation (Triangle 6), reporting, for each triangle–location pair, the detachment volume, the average distance traveled between the liquid inlet and attachment to the channel wall, and the number of droplets that coalesce prior to detachment. A consistent, location-dependent pattern emerges across all six triangular orientations. Droplets released at location 1 attain markedly larger detachment volumes (7.71–9.12 nL) and travel substantially greater distances prior to wall attachment (1600–3500 μm) than droplets released elsewhere, and in five of the six orientations this droplet coalesces with 2–4 neighboring droplets beforehand. Droplets released at locations 4 and 5 display the converse behavior: detachment volumes remain consistently small (4.03–5.96 nL), the attachment distance is short and narrowly distributed (200–300 μm), and no coalescence event is recorded at either location for any orientation. Droplets released at location 6 (and, where reported, location 7) occupy an intermediate regime, characterized by moderate-to-large volumes (6.43–9.33 nL) and a coalescence count that is invariably equal to two.

These systematic differences point to a location-dependent flow environment along the channel rather than a purely local effect of the triangular geometry. Location 1 evidently sits in a region where the local shear imposed by the crossflow is weakest —near the channel inlet—so that the droplet can grow substantially and travel a long distance while continuously entraining downstream neighbors before the accumulated aerodynamic loading finally exceeds the (also large, by this stage) capillary retention force. Locations ④ and ⑤, in contrast, are close to the sidewall surface, so that even a small droplet already experiences sufficient surface tension to detach quickly, before it has the opportunity to merge with adjacent droplets; the short and narrowly scattered attachment distances at these two locations support this interpretation. The consistent, non-zero merging count of exactly two droplets at location 6 for every triangle orientation suggests a geometrically fixed coupling with its immediate neighbor (location ⑦), independent of the upstream

inlet shape—i.e., locations ⑥ and ⑦ are close enough that their droplets reliably bridge and coalesce once either one begins to grow, regardless of triangle orientation.

Table 4. Under the triangular breakthrough shapes (Triangles 1–4 are equilateral triangles with different angles, and Triangles 5–6 are isosceles right triangles with different angles), the detachment volume and distance from the GDL surface of different droplets at different positions, combined with the number of droplets.

Operating Conditions	Location	Volume of Droplet (nL)—at Detachment	Average Distance Between Liquid Inlet and Attachment to Wall (μm)	Number of Merged Droplets
Triangle 1	1	7.71	2600	
	4	5.18	300	
	5	5.00	200	
	6	6.98		2
Triangle 2	1	9.12	3500	4
	4	5.65	200	2
	6	9.33		
	7	8.31		
Triangle 3	1	7.84	2000	3
	4	5.33	300	
	5	5.15	300	
	6	6.43		2
Triangle 4	1	7.91	2000	
	4	5.96	200	
	5	5.10	200	
	6	7.33		2
Triangle 5	1	8.48	1600	3
	4	4.74	200	
	5	4.16	200	
	6	6.84	2000	2
Triangle 6	1	7.79	1700	3
	2	6.97	100	
	4	4.03	200	
	5	4.64	200	
	6	6.77	1000	2

3.2.2. Circular, Square, Regular Pentagonal and Hexagonal Inlets

Under identical operating conditions (water inlet velocity of 0.0209 m s^{-1} and air velocity of 10 m s^{-1}, as reported in Figure 3), clear differences in droplet detachment behavior are observed among square, pentagonal, hexagonal, and circular breakthrough geometries. Circular inlets consistently exhibit the shortest detachment times, whereas polygonal inlets tend to retain droplets for longer durations.

Figure 6a ranks the mean detachment time of all inlet shapes examined from longest to shortest. Triangle 5 and Triangle 2 give the two longest detachment times (≈0.10 s); the pentagonal, hexagonal, Triangle 6, and Triangle 4 orientations cluster closely around ≈0.09 s, the two square orientations and Triangle 1/Triangle 3 fall to ≈0.083–0.086 s, and the circular inlet gives the shortest detachment time of the set (≈0.082 s). The associated error bars, which reflect the location-to-location scatter for each shape, overlap substantially between neighboring shapes, indicating that the ranking is a robust but not sharply separated trend.

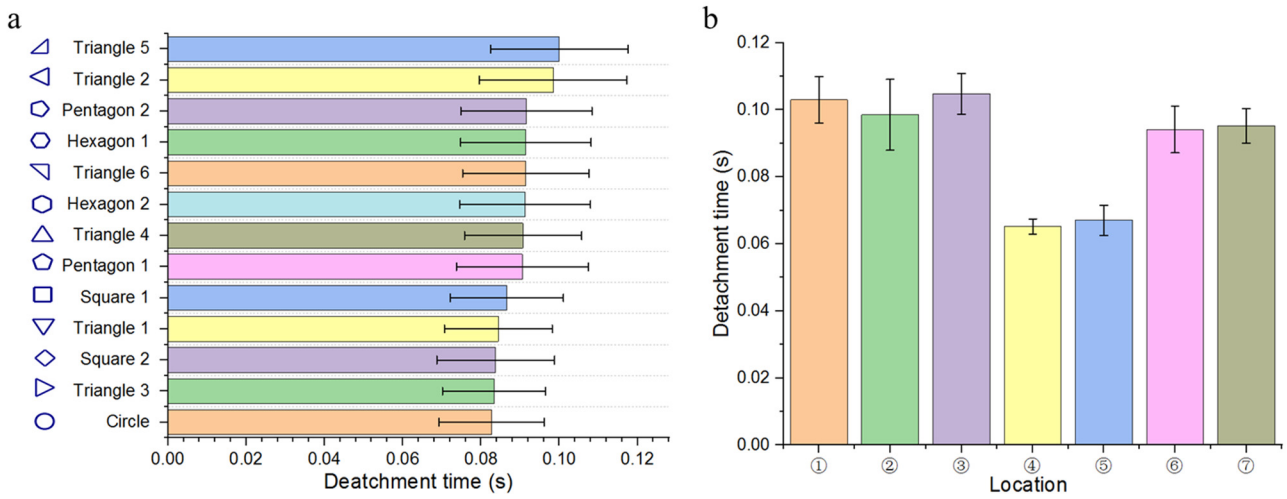

Figure 6. Comparative effect of inlet shape and breakthrough location on droplet detachment time. (**a**) Mean detachment time ranked across triangular (Triangle 1–6), square, pentagonal, hexagonal and circular breakthrough positions, with error bars indicating location-to-location scatter. (**b**) Detachment time resolved by breakthrough location (①–⑦) for a fixed reference inlet shape.

Figure 6b decomposes the detachment time by breakthrough location (①–⑦) for a fixed reference inlet shape, revealing that location, independent of shape, is itself a strong source of variability: locations ①, ② and ③ show the longest detachment times (≈0.10 s), locations ④ and ⑤ are markedly faster (≈0.065–0.067 s), and locations ⑥ and ⑦ return to an intermediate value (≈0.094–0.095 s). This pattern mirrors the location-dependent flow environment inferred from Table 4: the short detachment times at locations ④/⑤ are consistent with the locally accelerated crossflow proposed there, while the longer times at ①–③ are consistent with a weaker local shear. In Figure 6a, circular inlets minimize detachment time because their smoothly curved, continuously advancing windward interface builds up aerodynamic drag on the droplet fastest for a given growth rate, whereas polygonal and triangular perimeters introduce flat facets and corners that locally interrupt this build-up (by pinning the contact line or creating locally shielded regions in the droplet's lee), delaying the point at which drag exceeds capillary retention. Because this shape effect is superimposed on the larger, location-driven variability shown in Figure 2b, the two effects should be regarded as coupled rather than independent, and shape-optimization strategies for water removal should be evaluated location-by-location rather than from a single channel-averaged detachment time.

3.2.3. Engineering Implications of Breakthrough Geometry on Water Management

Breakthrough inlet geometry governs droplet interaction, detachment, and flow regimes in the PEFC gas channel. Symmetric shapes (e.g., circular) promote stable growth and early detachment, enhancing drainage, whereas asymmetric geometries (e.g., triangular) induce deformation and frequent small-droplet release. These behaviors arise from the balance between capillary retention and aerodynamic forces, consistent with LBM results showing geometry-dependent interfacial asymmetry [17]. From an engineering perspective, optimized geometries such as laser-structured smooth circular pores serving as drainage paths improve water removal and reduce oxygen transport losses, thereby enhancing cell performance [21,22].

4. Typical Force Analysis

To correct and clarify the mechanistic interpretation, four representative force scenarios are presented below with explicit reference to typical breakthrough geometries observed in

the present simulations. For each scenario, the dominant force components—streamwise inertial force $F_{p,x}$ in Equation (10), transverse aerodynamic force $F_{p,y}$ in Equation (11), and vertical/lift force $F_{p,z}$ in Equation (12) (the three forces are the three components of inertial force)—are identified, and the resultant interfacial dynamics are discussed. Other forces are one to three orders of magnitude smaller than the aerodynamic force; therefore, the analysis here focuses on the effects of the aerodynamic force.

4.1. Gas Channel Sidewall Flow

Figure 7 corresponds to droplets originating from triangular breakthrough geometries with an asymmetric windward orientation. For the second triangular inlet (② in Figure 7), the centroid of the breakthrough opening is located closer to the sidewall, causing the incoming air to preferentially bypass the upper surface of the droplet. This asymmetric bypassing generates a significant transverse aerodynamic inertial force in the negative Y-direction, often comparable to or even exceeding the streamwise component $F_{p,x}$. The dominant $F_{p,y}$ (-1.03×10^{-5} N; the negative sign indicates the negative direction of the y-axis) drives pronounced lateral deformation toward the wall and promotes sliding or sidewall-adhering trajectories. Early detachment, directed merging with nearby droplets, and rapid transition to corner flow are therefore frequently observed. This behavior confirms that the asymmetric contact-line distribution and wall proximity inherent to triangular inlets strongly amplify the sensitivity of detachment volume and detachment time to the inlet orientation.

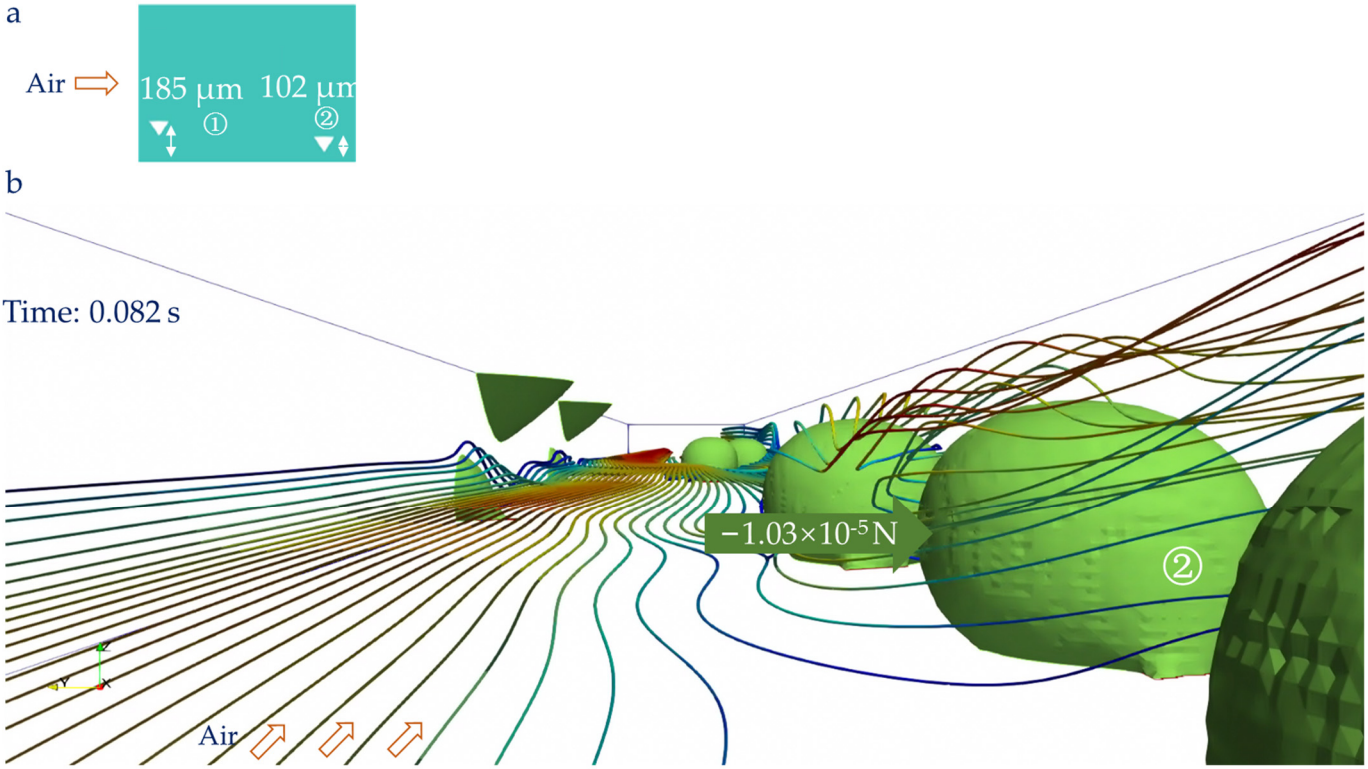

Figure 7. Force analysis of droplet sidewall flow. The direction of airflow is along the positive x-axis towards the inner side of the flow channel; the same applies below. (**a**) GDL pore type, position. (**b**) Droplet flow in the gas channel, streamlines.

4.2. Gas Channel Corner Flow

Figure 8 corresponds to breakthrough locations positioned close to the vertical gas channel wall. As the droplet grows, its expanding interface first makes contact with the wall. Because the wall surface is relatively hydrophilic, the local surface-tension forces promote

lateral spreading of the liquid along the wall, rather than allowing the droplet to maintain a compact shape. This wall-induced spreading produces a quasi-axisymmetric frontal interface, despite the asymmetric inlet geometry (Figure 8a, location ④). Consequently, the streamwise inertial force $F_{p,x}$ becomes the dominant aerodynamic component in Figure 8b,c, while the transverse and vertical forces remain small due to the stabilized, wall-flattened interface, as shown in Table 5.

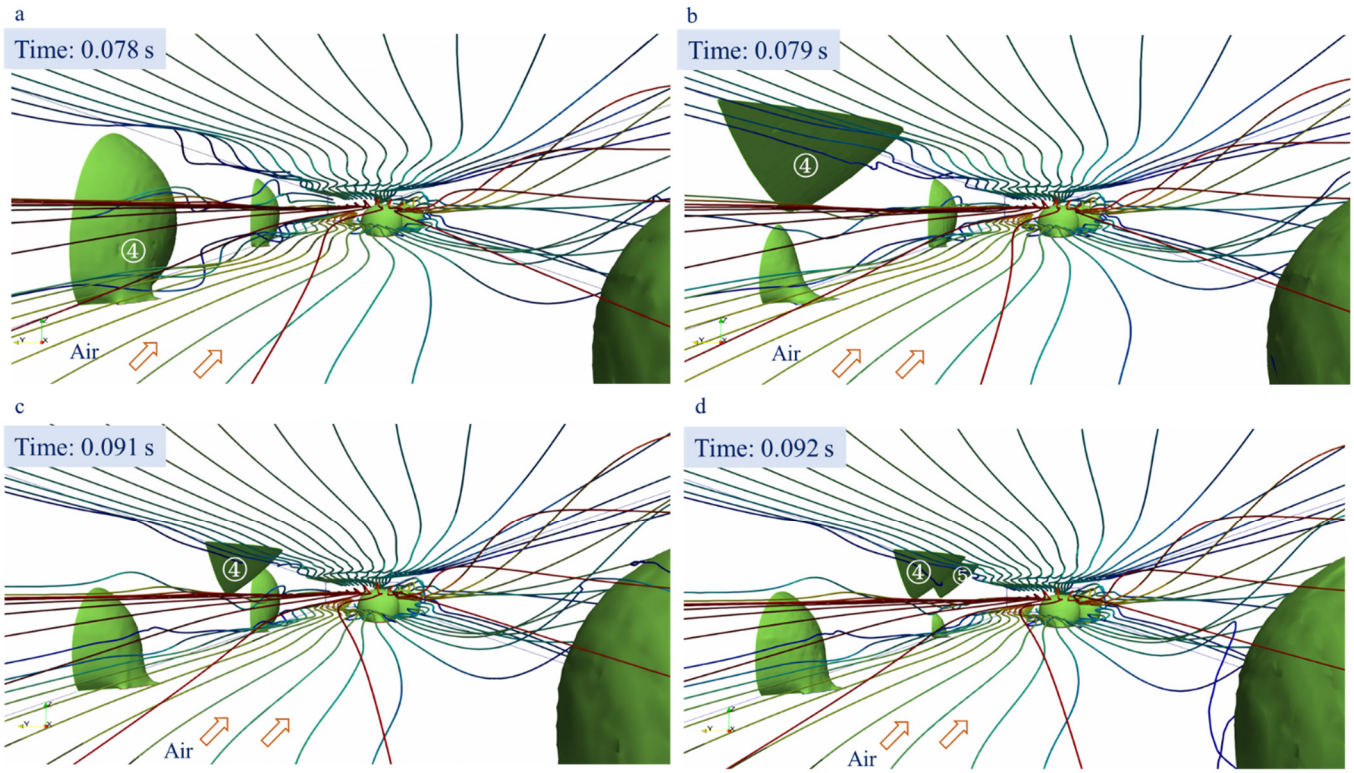

Figure 8. At different times, the droplet angular flow at the ④ and ⑤ breakthrough positions, and the streamlines flowing through the droplet towards the inner side of the flow channel. (**a**) 0.078 s, droplet at position ④; (**b**) 0.079 s, droplet at position ④; (**c**) 0.091 s, droplet at position ④; (**d**) 0.092 s, droplet at position ④ and ⑤

Table 5. Aerodynamic inertial force component table.

Time (s)	Location	$F_{p,x}$ (N)	$F_{p,y}$ (N)	$F_{p,z}$ (N)
0.078	④	3.41×10^{-7}	3.06×10^{-8}	1.09×10^{-6}
	⑤	4.36×10^{-7}	1.51×10^{-7}	4.48×10^{-7}
0.092	④	2.91×10^{-6}	1.21×10^{-6}	4.09×10^{-6}
	⑤	7.28×10^{-7}	1.61×10^{-7}	4.54×10^{-7}

The combination of wall contact and hydrophilic spreading results in gradual downstream stretching and highly repeatable detachment volumes and detachment times. Prior to detachment, the droplet evolves in a quasi-static manner, with capillary adhesion along the extended wall contact line counterbalancing $F_{p,x}$. Detachment finally occurs when $F_{p,x}$ exceeds this capillary retention in Figure 8b; the droplet moves (Figure 8c), and then coalescences (Figure 8d, droplets of location ④and location ⑤). This sequence—initial expansion, wall contact, hydrophilic spreading, and capillary-controlled evolution—explains the stable and predictable drainage behavior observed under different airflow conditions.

4.3. Flow on the Upper Wall of the Gas Channel

The scenario in Figure 9 occurs for droplets originating from circular breakthrough inlets that generate relatively smooth and symmetric initial interfaces. As the droplet grows, its volume eventually becomes large enough for the upper part of the interface to contact the gas channel ceiling. Once the liquid touches the upper wall, the surface-tension force at the ceiling–droplet contact line acts together with the aerodynamic vertical (lift) force $F_{p,z}$ to pull the droplet upward.

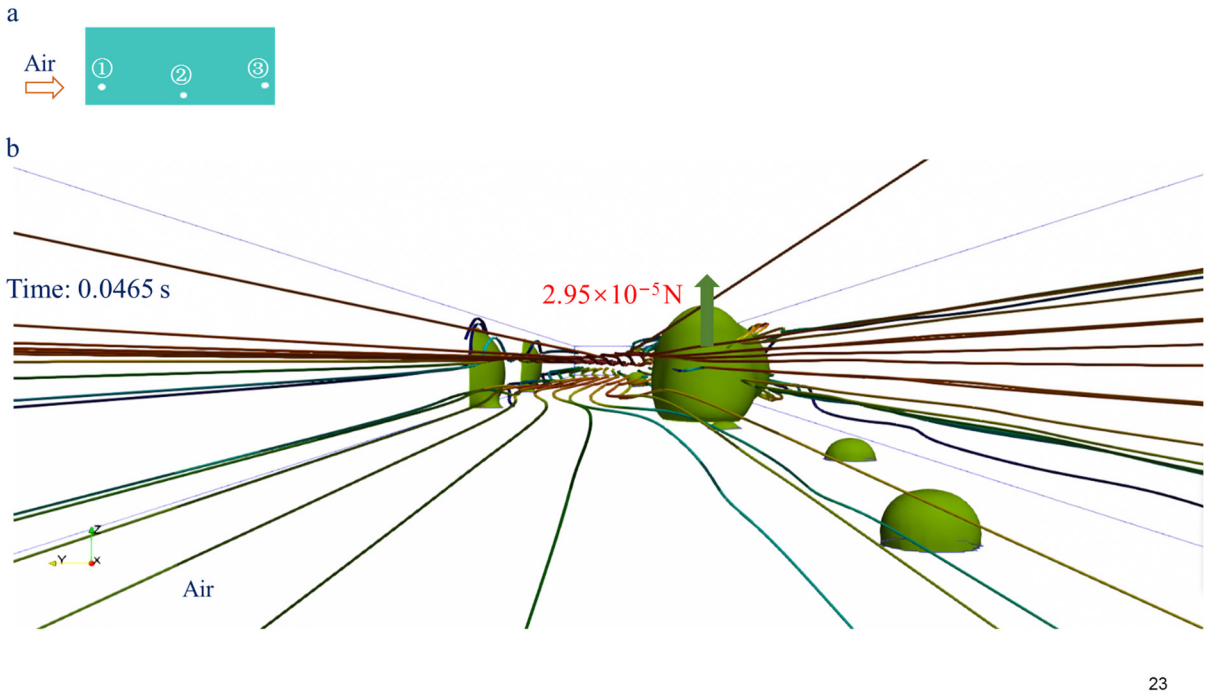

Figure 9. The droplets at the 1st to 3rd circular breakdown sites merge and flow onto the upper wall. (**a**) Location. (**b**) Streamlines in the gas channel bypass the droplet towards the inner side of the flow channel.

In this configuration, $F_{p,z}$ no longer acts solely to deform the interface but instead cooperates with the capillary adhesion at the upper wall. This combined action causes the droplet to migrate toward the ceiling, after which it can either spread along the upper wall or undergo upward detachment into the core flow, depending on the balance between $F_{p,z}$ and the capillary retention.

Because circular inlets produce relatively uniform interface curvature, the upward transition is governed primarily by droplet size and the oncoming gas flow rather than geometric irregularity. Once ceiling contact is established, the amplified vertical loading and capillary anchoring often lead to stable upper-wall sliding or the formation of elongated rivulets along the ceiling. This behavior represents a distinct lift-assisted, wall-contact-mediated transport mode.

4.4. Gdl-Surface Flow

Figure 10 shows a situation in regions near the downstream end of the gas channel, where multiple breakthrough points exist but their spacing and operating conditions do not favor droplet merging. In this regime, droplets remain relatively small and continue to move along the GDL surface without coalescing into a larger structure. As a result, the droplet volume never becomes large enough to reach or interact with the upper wall.

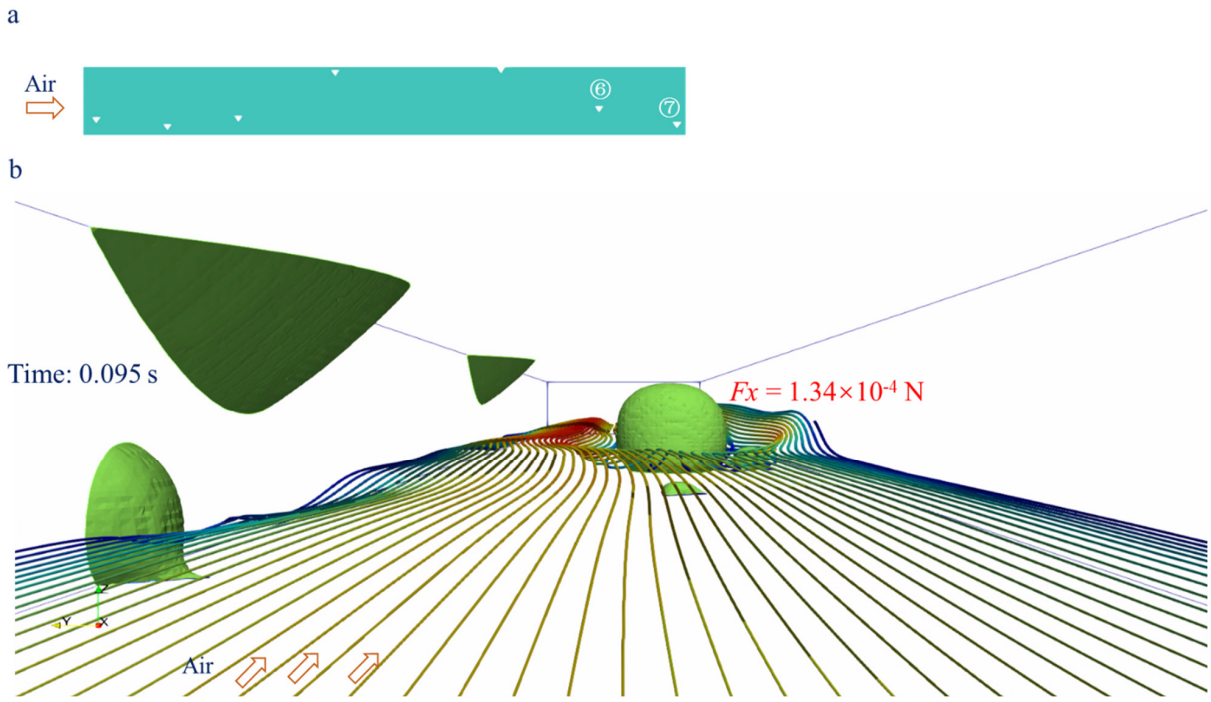

Figure 10. An equilateral triangle breakdown shape; the ⑥ and ⑦ droplets merge and flow onto the GDL surface. (**a**) The location of the ⑥ and ⑦ breakthroughs. (**b**) Streamlines in the gas channel bypass the droplet towards the inner side of the flow channel.

Under these conditions, none of the aerodynamic inertial force components—$F_{p,x}$, $F_{p,y}$, or $F_{p,z}$—is dominant. The streamwise force $F_{p,x}$ is largely balanced by capillary retention on the GDL, while moderate $F_{p,y}$ and $F_{p,z}$ only introduce minor perturbations. This balanced-force environment leads to extended residence time on the GDL, slight oscillation of the contact line, and persistent surface sliding rather than detachment or upward migration. The droplets therefore follow a relatively stable, surface-confined trajectory determined by the combined but moderate contributions of $F_{p,x}$, $F_{p,y}$, and $F_{p,z}$, without forming composite droplets or continuous rivulets.

Although the orders of magnitude of the forces acting on the droplets align with those reported by Niblett et al. [31], atomic force microscopy (AFM) or optical tweezers could be further employed to conduct an in-depth analysis of the forces and validate the simulation results.

5. Conclusions

This study conducted a comprehensive three-dimensional VOF simulation to investigate the effects of breakthrough geometry, operating conditions, and interfacial forces on two-phase flow behavior in a PEFC gas channel. The results demonstrate that liquid–gas interface evolution, droplet morphology, and drainage rate are highly sensitive to the inlet shape, air velocity, wettability, and the number of breakthrough sites.

The airflow velocity governs the overall drainage performance by directly modifying the balance between inertial and capillary forces. Higher air velocities accelerate droplet deformation and detachment, reduce the residence time on the GDL surface, and promote downstream transport or coalescence-driven removal. Conversely, reduced airflow leads to larger droplet volumes and delayed detachment. Breakthrough geometry was found to be equally important: circular and hexagonal openings provide stable and repeatable detachment behavior due to symmetric aerodynamic loading, whereas triangular or sharply edged inlets generate strong transverse or vertical force components, producing early

distortion, asymmetric trajectories, and frequent merging events. Breakthrough size, water injection velocity, and contact angle further influence the detachment volume and transition between surface flow, corner flow, and upper-wall sliding.

The force decomposition further clarifies the physical origins of the diverse droplet behaviors observed in this study. Four distinct force scenarios emerge across the different breakthrough conditions. (i) Transverse-force-dominated motion occurs for asymmetric triangular inlets whose proximity to the wall and upper-surface bypassing generate a strong negative-Y inertial component, producing lateral deformation and directed sliding. (ii) Streamwise-dominated detachment arises when droplets expand, contact the side-wall, and spread along the hydrophilic surface; the resulting quasi-axisymmetric interface stabilizes transverse and vertical forces, allowing $F_{p,x}$ to govern detachment in a highly predictable manner. (iii) Lift-assisted upward migration appears for large droplets formed at circular inlets once they reach the gas channel ceiling, where capillary adhesion at the upper wall works together with the vertical lift force $F_{p,z}$ to drive upward spreading or ceiling-attached rivulet formation. (iv) Balanced-force regimes occur near the downstream GDL surface where droplets remain small and do not merge; here $F_{p,x}$, $F_{p,y}$, and $F_{p,z}$ are comparable, suppressing detachment and maintaining a stable surface-sliding motion.

From an engineering perspective, the findings highlight fundamentally different water-management requirements on the cathode of PEFC. On the cathode, rapid and reliable drainage is essential to prevent oxygen transport limitations; therefore, breakthrough shapes that promote early detachment—such as circular openings—and higher local airflow are advantageous for minimizing gas channel blockage. Thus, the statistical distribution of breakthrough shapes and local wettability should be tailored independently on the cathode according to their contrasting water-management objectives.

Overall, this study provides a detailed mechanistic framework for understanding how microscale breakthrough geometries and interfacial forces regulate drainage kinetics and water distribution in the PEFC gas channel. The insights gained here offer guidance for the targeted design of GDL microstructures, breakthrough-shape distributions, and operating strategies to simultaneously enhance cathode drainage, thereby improving the durability and performance of next-generation PEFC.

Author Contributions: Conceptualization, D.L. and R.P.; methodology, D.L. and D.F.; software, D.L.; validation, D.L.; formal analysis, D.L.; investigation, D.L.; writing—original draft preparation, D.L.; writing—review and editing, D.F., Yanyu Chen and R.P.; supervision, R.P. All authors have read and agreed to the published version of the manuscript.

Funding: The authors acknowledge the financial support provided by the China Scholarship Council (CSC, Grant No. 202009370045).

Data Availability Statement: All raw data have been included in the paper; please contact the corresponding author if the source files for the simulations are required.

Acknowledgments: The computational resources were provided by the CLAIX high-performance computing system at RWTH Aachen University under the NHR4CES project (No. p0022420). Thanks to Christopher Wood for the English review.

Conflicts of Interest: The authors declare no conflict of interest.

References

1. Andersson, M.; Beale, S.; Espinoza, M.; Wu, Z.; Lehnert, W. A review of cell-scale multiphase flow modeling, including water management, in polymer electrolyte fuel cells. *Appl. Energy* **2016**, *180*, 757–778. [CrossRef]
2. Froning, D.; Brinkmann, J.; Reimer, U.; Schmidt, V.; Lehnert, W.; Stolten, D. 3D analysis, modeling and simulation of transport processes in compressed fibrous microstructures using the lattice Boltzmann method. *Electrochim. Acta* **2013**, *110*, 325–334. [CrossRef]

3. Froning, D.; Gaiselmann, D.; Reimer, U.; Brinkmann, J.; Schmidt, V.; Lehnert, W. Stochastic aspects of mass transport in gas diffusion layers. *Transp. Porous Media* **2014**, *103*, 469–495. [CrossRef]
4. Akhtar, N.; Qureshi, A.; Scholta, J.; Hartnig, C.; Messerschmidt, M.; Lehnert, W. Investigation of water droplet kinetics and optimization of channel geometry for PEM fuel cell cathodes. *Int. J. Hydrogen Energy* **2009**, *34*, 3104–3115. [CrossRef]
5. Arvay, A.; French, J.; Wang, J.C.; Peng, X.H.; Kannan, A.M. Nature-inspired flow field designs for proton exchange membrane fuel cells. *Int. J. Hydrogen Energy* **2013**, *38*, 3717–3726. [CrossRef]
6. Sharaf, O.Z.; Orhan, M.F. An overview of fuel cell technology: Fundamentals and applications. *Renew. Sustain. Energy Rev.* **2014**, *32*, 810–853. [CrossRef]
7. Guilizzoni, M.; Santini, M.; Lorenzi, M.; Knisel, V.; Fest-Santini, S. Micro-computed tomography and CFD simulation of drop deposition on gas diffusion layers. *J. Phys. Conf. Ser.* **2014**, *501*, 012028. [CrossRef]
8. Jiao, K.; Li, X. Water transport in polymer electrolyte membrane fuel cells. *Prog. Energy Combust. Sci.* **2011**, *37*, 221–291. [CrossRef]
9. Song, G.H.; Meng, H. Numerical modeling and simulation of PEM fuel cells: Progress and perspective. *Acta Mech. Sin.* **2013**, *29*, 318–334. [CrossRef]
10. Ji, M.; Wei, Z. A review of water management in polymer electrolyte membrane fuel cells. *Energies* **2009**, *2*, 1057–1106. [CrossRef]
11. Nabovati, A.; Hinebaugh, J.; Bazylak, A.; Amon, C.H. Effect of porosity heterogeneity on permeability and tortuosity of gas diffusion layers in polymer electrolyte membrane fuel cells. *J. Power Sources* **2014**, *248*, 83–90. [CrossRef]
12. Andersson, M.; Nakajima, H.; Kitahara, T.; Shimizu, A.; Koshiyama, T.; Paradis, H.; Yuan, J.; Sundén, B. Comparison of humidified hydrogen and partly pre-reformed natural gas as fuel for solid oxide fuel cells using computational fluid dynamics. *Int. J. Heat Mass Transf.* **2014**, *77*, 1008–1022. [CrossRef]
13. Wang, C.; Zhang, Q.; Lu, J.; Shen, S.; Yan, X.; Zhu, F.; Cheng, X.; Zhang, J. Effect of height- and width-tapered flow fields on polymer electrolyte membrane fuel cell performance. *Int. J. Hydrogen Energy* **2017**, *42*, 23107–23117. [CrossRef]
14. Cheah, M.J.; Kevrekidis, I.G.; Benziger, J.B. Water slug-to-drop and film transitions in gas-flow channels. *Langmuir* **2013**, *29*, 15122–15131. [CrossRef] [PubMed]
15. Hussaini, I.S.; Wang, C.Y. Visualization and quantification of cathode channel flooding in PEM fuel cells. *J. Power Sources* **2009**, *187*, 444–451. [CrossRef]
16. Wu, T.C. Two-Phase Flow in Microchannels with Application to PEM Fuel Cells. Ph.D. Thesis, University of Victoria, Victoria, BC, Canada, 2015.
17. Yu, J.; Froning, D.; Reimer, U.; Lehnert, W. Apparent contact angles of liquid water droplets breaking through a gas diffusion layer of polymer electrolyte membrane fuel cells. *Int. J. Hydrogen Energy* **2018**, *43*, 6318–6330. [CrossRef]
18. Andersson, M.; Beale, S.; Reimer, U.; Lehnert, W.; Stolten, D. Interface-resolving two-phase flow simulations in gas channels relevant for polymer electrolyte fuel cells using the volume of fluid approach. *Int. J. Hydrogen Energy* **2018**, *43*, 2961–2976. [CrossRef]
19. Andersson, M.; Mularczyk, A.; Lamibrac, A.; Beale, S.B.; Eller, J.; Lehnert, W.; Büchi, F.N. Modeling and synchrotron imaging of droplet detachment in gas channels of polymer electrolyte fuel cells. *J. Power Sources* **2018**, *404*, 159–169. [CrossRef]
20. Yu, J.; Froning, D.; Reimer, U.; Lehnert, W. Polytetrafluoroethylene effects on liquid water flowing through the gas diffusion layer of polymer electrolyte membrane fuel cells. *J. Power Sources* **2019**, *438*, 227000. [CrossRef]
21. Horst, R.J.; van der Linde, R.; Jacquemond, R.R.; Liu, B.; Forner-Cuenca, A. Designer diffusion media microstructures enhance polymer electrolyte fuel cell performance. *Energy Environ. Sci.* **2025**, *18*, 10061–10077. [CrossRef] [PubMed]
22. Peng, Q.; Xu, H.; He, Y.; Jiang, Y.; Wu, Z.; Zhang, Y.; Liao, Q. Aligned-pore engineering: Decoupling gas–liquid transport in gas diffusion electrodes. *Joule* **2025**, *9*, 12. [CrossRef]
23. Lv, X.; Zhou, Z.; Wu, W.-T.; Wei, L.; Gao, L.; Lyu, J.; Hu, C.; Li, Y.; Li, Y.; Song, Y. Investigation of droplet dynamic in PEMFCs gas diffusion layer and gas channel with Micro-CT and lattice Boltzmann method. *Fuel* **2025**, *381*, 133677. [CrossRef]
24. Aroge, F.A.; Parimalam, B.S.; MacDonald, J.A.; Orfino, F.P.; Dutta, M.; Kjeang, E. Analysing operando 2D X-ray transmission images for liquid water distribution in polymer electrolyte fuel cells. *J. Power Sources* **2023**, *564*, 232820. [CrossRef]
25. Pei, H.; Xiao, C.; Tu, Z. Experimental study on liquid water formation characteristics in a novel transparent proton exchange membrane fuel cell. *Appl. Energy* **2022**, *321*, 119349. [CrossRef]
26. Hirt, C.W.; Nichols, B.D. Volume of fluid (VOF) method for the dynamics of free boundaries. *J. Comput. Phys.* **1981**, *39*, 201–225. [CrossRef]
27. Le, A.D.; Zhou, B. A general model of proton exchange membrane fuel cells. *J. Power Sources* **2008**, *182*, 197–206. [CrossRef]
28. Carton, J.G.; Lawlor, V.; Olabi, A.G.; Hochenauer, C.; Zauner, G. Water droplet accumulation and motion in PEM fuel cell mini-channels. *Appl. Energy* **2012**, *39*, 63–73. [CrossRef]
29. Jo, J.H.; Kim, W.T. Numerical simulation of water droplet dynamics in a right-angle gas channel of a polymer electrolyte membrane fuel cell. *Int. J. Hydrogen Energy* **2015**, *40*, 8368–8383. [CrossRef]
30. Qin, C.Z. Numerical Investigations on Two-Phase Flow in Polymer Electrolyte Fuel Cells. Ph.D. Thesis, Uppsala University, Uppsala, Sweden, 2012.

31. Niblett, D.; Holmes, S.M.; Niasar, V. Discrete-particle model to optimize operational conditions of proton-exchange membrane fuel cell gas channels. *Adv. Appl. Energy Mater.* **2021**, *4*, 10514. [CrossRef] [PubMed]
32. Yu, J.; Froning, D.; Reimer, U.; Lehnert, W. Liquid water breakthrough location distances on a gas diffusion layer of polymer electrolyte membrane fuel cells. *J. Power Sources* **2018**, *389*, 56–60. [CrossRef]
33. Yu, J. Lattice Boltzmann Simulation in Components of Polymer Electrolyte Fuel Cells. Ph.D. Thesis, RWTH Aachen University, Aachen, Germany, 2018.
34. Andersson, P.; Andric, J.; Rynell, A. *Tutorial: Multiphaseinterfoam*; Chalmers University of Technology: Gothenburg, Sweden, 2010.
35. OpenFOAM Foundation. OpenFOAM v11 [Software]. Available online: https://openfoam.org/ (accessed on 29 January 2026).